An Improved Generalized Extended State Observer for Current Harmonic Compensation in Dual Three-Phase PMSMs

Xuefeng Zhang, *Student Member, IEEE*, Qiwei Xu, Yiru Miao, Xuan Wu, Yiming Wang, *Student Member, IEEE*, and Liangwu Yi

***Abstract*—Dual three-phase permanent magnet synchronous machine (DTP-PMSM) suffers from the disadvantage of easily occurring large stator current harmonics under inverter nonlinearity, nonsinusoidal back-electromotive force, and external disturbances. To deal with the problem, an improved generalized extended state observer (IGESO) for current harmonic suppression is proposed in this article. First, the relationship between the observation of low-frequency and high-frequency periodic disturbances in conventional disturbance observers is explored. Second, a notch filter is used to optimize the conventional generalized extended state observer (GESO) structure to avoid interference in observing two different frequency disturbances. Then, a novel observer poles design principle is proposed, which can control the suppression frequency range and attenuation of periodic disturbances respectively. Besides, the performance compared with other strategies and the stability analysis of IGESO in the discrete-time domain are presented. The parameter range for system stability is also provided. Finally, the proposed method is evaluated on a laboratory DTP-PMSM platform.**

***Index Terms*—Current control, dual three-phase permanent magnet synchronous machine (PMSM), extended state observer (ESO), harmonics.**

I. Introduction

MULTIPHASE motors have the advantages of smaller torque pulsation, lower harmonics of dc link current, and better fault-tolerant capacity compared with conventional three-phase permanent magnet synchronous machines (PMSMs) [1], [2]. One of the most widely used multiphase machine structures is the Dual three-phase (DTP)-PMSM due to its utilization of two sets of standard three-phase windings [3]. Currently, DTP-PMSMs have two structures: a symmetrical type with two sets of three-phase windings shifted by 60° and an asymmetrical type with two sets shifted by 30°. There is more attention among researchers and industry to the asymmetrical configuration because of the inherent advantage of the sixth-order torque ripple elimination [4], [5].

The magnetic coupling of DTP-PMSM is more complex than that of the PMSM. Through the vector space decomposition (VSD) method, the fundamental components can be mapped into the two orthogonal subspaces, α–β and x–y, thereby achieving decouple control of the motor [6]. However, the impedance in x–y subspace consists of phase resistance and leakage inductance, which is much smaller than the α–β subspace. Thus, even a small harmonic voltage could result in large harmonic currents [7]. The primary sources of disturbances include inverter nonlinearity, flux harmonics, winding asymmetry, modulation strategies, and magnetic circuit saturation [8], [9]. Large stator current harmonics can cause harmonic losses, reduce the system efficiency, and may degrade the performance of some methods [10]. This limits the extended application of DTP-PMSMs in the industry. As such, solutions to harmonic currents are strongly desirable for DTP-PMSM drives. These methods can be divided into two main categories, one is to make the x–y subspace voltages zero, and the other is to improve the current controller in x–y subspace.

The first type of method is most common in model-based predictive current control, especially with the finite-control-set [11], [15]. The methods with virtual vectors (VVs) have been widely adopted, which produce an average zero x–y voltages [11], [12]. However, the use of VVs not only reduces the voltage range of α–β subspace [13], [14], but also has limited harmonic suppression ability due to its open-loop control [15], [16].

The second type of method is more effective. The multifrequency proportional-resonant (PR) control has been developed to eliminate the current harmonics [4]. However, anomalous peaks caused by phase lag will degrade performance [17]. To simplify the implementation, multiple synchronous reference frames (MSRFs) have been used, which convert ac signals into dc signals so that they can be adjusted by the proportional-integral (PI) controller [18]. Low-pass filters (LPFs) are inevitable in MSRF to prevent the ac components' impact on the PI

Received 4 July 2024; revised 15 November 2024; accepted 28 December 2024. Date of publication 7 January 2025; date of current version 26 February 2025. This work was supported in part by the Project of Nuclear Power Technology Innovation Center of Science Technology and Industry for Nation Defense of China under Grant HDLCXZX-2021-ZH-016, and in part by the Natural Science Foundation of Chongqing under Grant CSTB2022NSCQ-MSX0430. Recommended for publication by Associate Editor K. Akatsu. *(Corresponding author: Yiru Miao.)*

Xuefeng Zhang, Qiwei Xu, Yiru Miao, Yiming Wang, and Liangwu Yi are with the State Key Laboratory of Power Transmission Equipment Technology, Chongqing University, Chongqing 400044, China (e-mail: zhangxf07x@cqu.edu.cn; xuqw@cqu.edu.cn; miaoyiru@cqu.edu.cn; wangym@cqu.edu.cn; liangwuyi@stu.cqu.edu.cn).

Xuan Wu is with the College of Electrical and Information Engineering, Hunan University, Changsha 410082, China (e-mail: wuxuan@hnu.edu.cn).

Color versions of one or more figures in this article are available at https://doi.org/10.1109/TPEL.2025.3526624.

Digital Object Identifier 10.1109/TPEL.2025.3526624

feedback signal, but LPFs will cause poor dynamic performance and instability. To avoid LPFs, a virtual multithree-phase system with more three-phase sets is established [19], which can decompose the current harmonics into several isolated subspaces.

Separating current tracking and disturbance suppression to form a two-degree-of-freedom (2DOF) controller can effectively improve the performance of the current controller [20], [21]. An inverse-model-based disturbance observer (DOB) is proposed for DTP-PMSM in [10]. However, only sixth voltage harmonics are suppressed due to the design of the Q filter. The extended state observer (ESO) proposed in [22] can estimate lumped disturbances and has been extensively investigated and applied. In [23], a linear ESO is used in DTP-PMSM, and the superiority of ESO in harmonic suppression compared to PR is analyzed in the frequency domain. However, the estimation error increases in first-order ESO as the frequency of periodic disturbance increases [24]. The higher-order ESO can improve estimation accuracy, but the bandwidth must be sufficiently larger than the disturbance frequency. The stability margins will also be reduced [25]. In addition, the bandwidth is limited by the measurement noise and the sampling frequency [26].

To solve these issues, the resonant term is involved in DOB. In [27], a generalized integral resonance disturbance observer is designed to compensate the position estimation error. In [28], a quasi-resonant extended state observer (QRESO) is proposed to improve the gain of the observer around the resonant frequency. In [29], a frequency adaptive law is proposed to obtain the resonant frequency of the observer so that it can estimate the uncertain periodic disturbances. However, they did not analyze the relationship between the observation of low-frequency disturbances and high-frequency periodic disturbances. In addition, it seems that no attempt has been made to suppress the harmonic currents in DTP-PMSM based on GESO.

Hence, this article goes one step further and proposes an IGESO for DTP-PMSMs drives. The proposed IGESO can not only suppress low-frequency and periodic current harmonics at the same time, but also reduce the interaction between different frequency disturbance observations. Moreover, a pole assignment method is proposed to design parameters independently and each parameter has a clear physical meaning. IGESO is allowed to control suppression frequency range and attenuation of periodic disturbances. The main contributions of this work are as follows.

1) Analyzing the observational impacts between low-frequency and periodic disturbances in terms of observer bandwidth and disturbance frequency variations.
2) Proposition of an IGESO-based current control for DTP-PMSM that can suppress low-frequency and periodic current harmonics at the same time.
3) Proposition of a pole assignment method that reduces the interaction between different frequency disturbance observations and eases the implementation and tuning of the observer;
4) Comparing performance with other strategies and analyzing the stability of discretized observer.

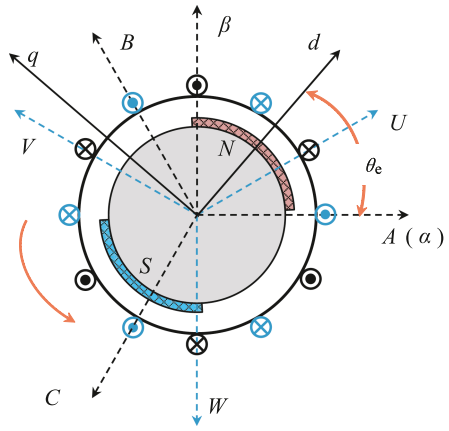

Fig. 1. Phase winding diagram for DTP-PMSM.

The rest of this article is organized as follows. Section II presents the machine model and harmonic analysis of the DTP-PMSM. Section III details the theory, design, and performance analysis of IGESO. Section IV gives the stability analysis in the discrete-time domain. The experimental results are provided in Section V. Finally, Section VI concludes this article.

II. System Model

A. Mathematical Model of DTP-PMSM

The stator windings of the DTP-PMSM are composed of two sets of three-phase windings offset by an electrical angle of 30°, and each set is separated from the neutral points. These sets are called the *ABC* and *UVW* windings, respectively, illustrated in Fig. 1.

With the VSD theory [6], each variable of DTP-PMSM can be transformed into three orthogonal subspaces: the α–β subspace, x–y subspace and o_1–o_2 subspace. The α–β subspace is related to the electromechanical energy conversion in the motor. Conversely, the x–y subspace is a harmonic subspace, which does not contribute to the energy conversion but induces the energy loss. Due to the neutral point isolation of the DTP-PMSM, the currents in the o_1–o_2 subspace are zero, which can be neglected. The VSD coordinate transformation matrix $T_{\alpha\beta}$ can be expressed as

$$\mathbf{T}_{\alpha\beta} = \frac{1}{3}\begin{bmatrix} 1 & -1/2 & -1/2 & \sqrt{3}/2 & -\sqrt{3}/2 & 0 \\ 0 & \sqrt{3}/2 & -\sqrt{3}/2 & 1/2 & 1/2 & -1 \\ 1 & -1/2 & -1/2 & -\sqrt{3}/2 & \sqrt{3}/2 & 0 \\ 0 & -\sqrt{3}/2 & \sqrt{3}/2 & 1/2 & 1/2 & -1 \end{bmatrix}. \tag{1}$$

Different order harmonics are mapped into different subspaces. The fundamental wave and harmonics with the order $12k \pm 1 (k = 1, 2, 3, \ldots)$ are mapped into the α–β subspace, whereas the harmonics with the order $6k \pm 1 (k = 1, 3, 5, \ldots)$ are mapped into the x–y subspace.

Similar to conventional three-phase PMSMs, the rotation transformation can be utilized to transform the α–β and x–y frame into d–q and dz–qz synchronous reference frames. The

rotation transformation matrix T_{dq} is

$$\begin{aligned}\mathbf{T}_{dq}(\theta_{\mathrm{e}}) &= \begin{bmatrix}\mathbf{T}_p(\theta_{\mathrm{e}}) & \mathbf{0}\\ \mathbf{0} & \mathbf{T}_p(-\theta_{\mathrm{e}})\end{bmatrix}\\ \mathbf{T}_p(\theta_{\mathrm{e}}) &= \begin{bmatrix}\cos\theta_{\mathrm{e}} & \sin\theta_{\mathrm{e}}\\ -\sin\theta_{\mathrm{e}} & \cos\theta_{\mathrm{e}}\end{bmatrix}\end{aligned} \tag{2}$$

where θ_e is the rotor position in electric angle. Then, the mathematical model of an ideal DTP-PMSM in the synchronous reference frame can be expressed as

$$\begin{cases} u_d = R_s i_d + L_d \frac{\mathrm{d}i_d}{\mathrm{d}t} - \omega_{\mathrm{e}} L_q i_q \\ u_q = R_s i_q + L_q \frac{\mathrm{d}i_q}{\mathrm{d}t} + \omega_{\mathrm{e}} L_d i_d + \omega_{\mathrm{e}} \psi_m \\ u_{dz} = R_s i_{dz} + L_{dz} \frac{di_{dz}}{dt} + \omega_{\mathrm{e}} L_{qz} i_{qz} \\ u_{qz} = R_s i_{qz} + L_{qz} \frac{di_{qz}}{dt} - \omega_{\mathrm{e}} L_{dz} i_{dz} \end{cases} \tag{3}$$

$$T_e = 3n_p\left[\psi_m + (L_d - L_q)\, i_d\right] i_q \tag{4}$$

where u, i, and T_e are the voltage, current, and torque, respectively. R_s is the stator resistance, L is the stator inductance, and ψ_m is the rotor flux linkage. ω_e is the electrical angular speed of the rotor, and n_p is the pole pair number of the motor. The subscript d and q denote the d- and q-axis, while the subscript dz and qz denote the dz- and qz-axis.

According to [30], the inductance of the harmonic subspace equals the stator leakage inductance L_σ. Hence, the same harmonic voltage would produce a larger harmonic current compared to the d–q subspace. Although the harmonic currents in the dz–qz subspace do not cause the torque ripple as (4), they cause additional losses and deteriorate the control performance.

B. Harmonic Disturbance of Current Control

In a practical motor drive system, the current control of the DTP-PMSM is affected by both internal and external disturbances. Harmonic disturbances mapped into the dz–qz subspace can originate from various sources, as follows.

1) Inverter nonlinearity. Dead time is essential in voltage source inverters [31]. Based on (1) and (2), the harmonic distortion voltage mapped into the dz–qz subspace can be expressed as

$$\begin{cases} \Delta u_{dz} = \frac{4M}{\pi} \sum\limits_{k=1}^{\infty} \frac{(24k-12)\sin[(12k-6)\omega_e t]}{144k^2-144k+35} \\ \Delta u_{qz} = \frac{4M}{\pi} \sum\limits_{k=1}^{\infty} \frac{2\cos[(12k-6)\omega_e t]}{144k^2-144k+35} \end{cases} \tag{5}$$

where M is a constant depending on the hardware and the length of dead time [31]. From (5), the magnitude of the voltage harmonic component decreases rapidly as the harmonic order increases. Therefore, in the dz–qz subspace, harmonics of 18th and higher orders can be ignored.

2) Flux harmonics. It is commonly assumed that the magnetic field of a permanent magnet exhibits an ideal sinusoidal distribution in space. However, nonidealities such as stator slotting, possible magnetic saturation, and pole shape would cause the fifth and seventh flux harmonics in the air gap [32]. ψ_{mdz} and ψ_{mqz} represent the mappings of the magnetic flux harmonics into the dz–qz subspace, which can be expressed as

$$\begin{cases} \psi_{mdz} = \sum\limits_{k=1}^{\infty} \psi_{mdz,k} \cos\left[(12k-6)\,\omega_e t\right] \\ \psi_{mqz} = \sum\limits_{k=1}^{\infty} \psi_{mqz,k} \sin\left[(12k-6)\,\omega_e t\right] \end{cases} \tag{6}$$

where $\psi_{mdz,k}$ and $\psi_{mqz,k}$ are the amplitudes of the $(12k-6)$th order flux harmonic. However, only the sixth-order flux harmonic is likely to cause harmonic currents in practical applications [32].

The abovementioned periodic disturbance, together with unmodeled disturbance as the lumped disturbance f_{dz_total} and f_{qz_total} in the input channel. Therefore, the nominal model of the dz–qz subspace can be expressed as

$$\begin{cases} \frac{di_{dz}}{dt} = a_0 i_{dz} + b_0 \left(u_{dz} + \frac{1}{b_0} f_{dz\_\mathrm{total}}\right) \\ \frac{di_{qz}}{dt} = a_0 i_{qz} + b_0 \left(u_{qz} + \frac{1}{b_0} f_{qz\_\mathrm{total}}\right) \end{cases} \tag{7}$$

where $a_0 = -R_{s0}/L_{\sigma 0}, b_0 = 1/L_{\sigma 0}$, R_{s0} and $L_{\sigma 0}$ represent the nominal value of R_s and L_σ, respectively. f_{dz_total} and f_{qz_total} can be expressed as

$$\begin{cases} f_{dz\_\mathrm{total}} = \Delta a \cdot i_{dz} + \Delta b \cdot u_{dz} - \omega_e i_{qz} \\ \qquad\qquad + b \cdot \Delta u_{dz} - b\omega_e \varphi_{mdz} \\ f_{qz\_\mathrm{total}} = \Delta a \cdot i_{qz} + \Delta b \cdot u_{qz} + \omega_e i_{dz} \\ \qquad\qquad + b \cdot \Delta u_{qz} - b\omega_e \varphi_{mqz} \end{cases} \tag{8}$$

where $\Delta a = -R_s/L_\sigma - a_0$ and $\Delta b = b - b_0 = 1/L_\sigma - b_0$. When the motor is operating stably, the disturbances caused by parameter mismatch, inverter nonlinearity, and back electromotive force harmonics are consistent with the current form, manifested as a combination of low-frequency slow varying disturbance and six-order periodic disturbance. Therefore, the lumped disturbance f_{total} can be modeled as

$$f_{\mathrm{total}}(t) = \underbrace{M_0}_{f_0(t)} + \underbrace{M_{6\omega}\cos(6\omega_e t + \varphi)}_{f_{6\omega}(t)} \tag{9}$$

where M_0 denotes the low-frequency slow-changing disturbance. $M_{6\omega}$ and φ are the amplitude and phase of the sixth harmonic, respectively. The dynamic characteristics of the disturbance $f_{6\omega}(t)$ can be derived as

$$\begin{cases} f_{6\omega}(t) = M_{6\omega}\cos(6\omega_e t + \varphi) \\ \frac{\mathrm{d}}{dt} f_{6\omega}(t) = \gamma(t) \\ \frac{\mathrm{d}}{dt}\gamma(t) = -(6\omega_e)^2 f_{6\omega}(t). \end{cases} \tag{10}$$

III. Design and Analysis of ESO

A. Design and Limitation of Traditional ESO

The ESO of the qz-axis current loop can be designed as

$$\begin{cases} \frac{d}{dt}\hat{i}_{qz} = a_0 \hat{i}_{qz} + b_0 u_{qz} + \hat{f}_{qz\_\mathrm{total}} + l_1\left(i_{qz} - \hat{i}_{qz}\right) \\ \frac{d}{dt}\hat{f}_{qz\_\mathrm{total}} = l_2\left(i_{qz} - \hat{i}_{qz}\right) \end{cases} \tag{11}$$

where symbol " $\hat{}$ " denotes the estimated value of the corresponding state variable, l_1 and l_2 are the gains of the ESO observer. The bandwidth parameterization method [33] is used to determine these gains. Hence, the gains in ESO can be calculated

by $l_1 = 2\omega_0, l_2 = {\omega_0}^2$. ω_0 denotes the bandwidth of ESO and it determines the performance of the observer.

According to (7) and (11), the transformation of the current estimation error $\widetilde{i}_{qz}(s)$ and disturbance estimation error $\widetilde{f}_{qz\_total}(s)$ into s-domain is derived as

$$\begin{cases} \widetilde{i}_{qz}(s) = \frac{s}{\Phi_1(s)} f_{qz\_total}(s) \\ \widetilde{f}_{qz\_total}(s) = \frac{s(s+2\omega_0)}{\Phi_1(s)} f_{qz\_total}(s) \end{cases} \tag{12}$$

where the symbol "~" denotes the error value of the corresponding state variable, calculated as the actual value minus the estimated value. $\Phi_1(s)$ is the characteristic equation, expressed as $\Phi_1(s) = (s+\omega_0)^2$.

From (12), it is obvious that the stability of the observer can be guaranteed. There is a zero point at the frequency of zero. That is, the dc component of the disturbance can be fully observed. Similar results can be obtained if the change rate of the disturbance is reasonably small. However, if the disturbance contains fast varying components, the performance of ESO designed as (11) can not offer satisfactory results.

B. Design of ESO Considering Disturbance Periodicity

Based on (7) and combined with the dynamic characteristics of disturbance, divide the qz-axis total disturbances $f_{qz\_total}(s)$ into low-frequency disturbances $f_{qz0}(t)$ and sixth-order disturbances $f_{qz6\omega}(t)$. The GESO can be designed as

$$\begin{cases} \frac{d}{dt}\hat{i}_{qz} = a_0\hat{i}_{qz} + b_0 u_{qz} + \hat{f}_{qz0} + \hat{f}_{qz6\omega} + l_1\left(i_{qz} - \hat{i}_{qz}\right) \\ \frac{d}{dt}\hat{f}_{qz0} = l_2\left(i_{qz} - \hat{i}_{qz}\right) \\ \frac{d}{dt}\hat{f}_{qz6\omega} = \hat{\gamma}(t) + l_3\left(i_{qz} - \hat{i}_{qz}\right) \\ \frac{d}{dt}\hat{\gamma}(t) = -(6\omega_e)^2\hat{f}_{qz6\omega} + l_4\left(i_{qz} - \hat{i}_{qz}\right) \end{cases} \tag{13}$$

where l_1, l_2, l_3, and l_4 are the observer gains. Compared to the observer designed in (11), the GESO adds two additional state variables to observe periodic disturbances. From (13), the characteristic polynomial of the observer is derived as

$$\begin{aligned} \Phi_2(s) = {} & s^4 + (l_1 - a_0)\, s^3 + \left(36\omega_e^2 + l_2 + l_3\right) s^2 \\ & + \left(-36a_0\omega_e^2 + 36l_1\omega_e^2 + l_4\right) s + \left(36l_2\omega_e^2\right). \end{aligned} \tag{14}$$

According to the bandwidth parameterization, set the roots of characteristic polynomial all fall at $-\omega_0$, that is, $\Phi_2(s) = (s+\omega_0)^4$. Thus, the gains in GESO can be obtained as

$$\begin{cases} l_1 = 4\omega_0 + a_0 \\ l_2 = \frac{\omega_0^4}{36\omega_e^2} \\ l_3 = 6\omega_0^2 - 36\omega_e^2 - \frac{\omega_0^4}{36\omega_e^2} \\ l_4 = 4\omega_0^3 - 36\omega_e^2 \cdot 4\omega_0 \end{cases}. \tag{15}$$

According to (7), (10), and (13), the observation error in s-domain can be derived as

$$\begin{cases} \widetilde{i}_{qz}(s) = \frac{\widetilde{f}_{qz0}(s) + \widetilde{f}_{qz6\omega}(s)}{s - a_0 + l_1} \\ \widetilde{f}_{qz0}(s) = f_{qz0}(s) - \frac{l_2}{s}\widetilde{i}_{qz}(s) \\ \widetilde{f}_{qz6\omega}(s) = f_{qz6\omega}(s) - \frac{sl_3 + l_4}{36\omega_e^2 + s^2}\widetilde{i}_{qz}(s) \end{cases}. \tag{16}$$

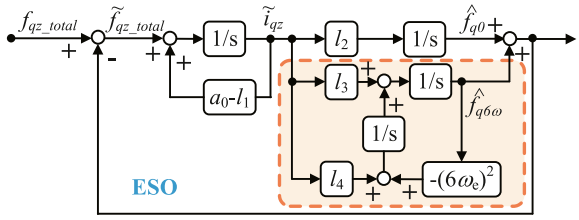

Fig. 2. Overall control system with the inner DOB loop.

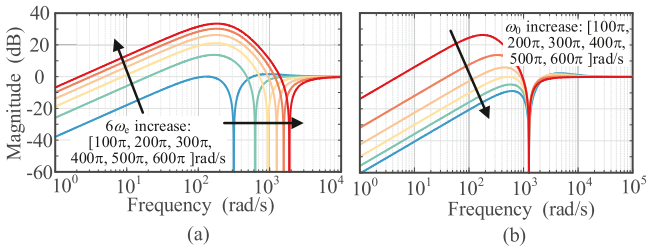

Fig. 3. Magnitude plot of sensitivity function. (a) Various $6\omega_e$, $\omega_0 = 100\pi$ rad/s. (b) Various ω_0, $6\omega_e = 400\pi$.

From (13) and (16), the GESO can be simplified to an equivalent unity-feedback system, as shown in Fig. 2. The current estimation error $\widetilde{i}_{qz}(s)$ and lumped disturbance estimation error $\widetilde{f}_{qz\_total}(s)$ can be derived as

$$\begin{cases} \widetilde{i}_{qz}(s) = \frac{s\left(s^2+36\omega_e^2\right)}{(s+\omega_0)^4} f_{qz\_total}(s) \\ \widetilde{f}_{qz\_total}(s) = \frac{s\left(s^2+36\omega_e^2\right)(s+4\omega_0)}{(s+\omega_0)^4} f_{qz\_total}(s) \end{cases}. \tag{17}$$

Compared with the estimation error of ESO in (12), the transfer function of GESO estimation error has additional zeros at $\pm j6\omega_e$. Therefore, the GESO can track fast-varying sixth-order sinusoidal disturbances. However, as demonstrated by the GESO model in (13), both $\hat{f}_{qz0}$ and $\hat{f}_{qz6\omega}$ estimates rely on the same current estimation error $\widetilde{i}_{qz}$ as input, which may result in mutual influence. In addition, as ω_e increases, the zeros at $(0, \pm j6\omega_e)$ are far away from the poles at $(-\omega_0, 0)$. The changes in the relative positions of zeros and poles can affect the dynamic performance of the observer. Therefore, fixed poles are not a good parameter configuration method.

The frequency analysis method can be used to explain the above issues. From Fig. 2, the sensitivity function $S_d(s)$, defined as $S_d(s) = \widetilde{f}_{qz\_total}(s)/f_{qz\_total}(s)$, represents the disturbance observation performance of the GESO. The magnitude plot of $S_d(s)$ under various $6\omega_e$ and ω_0 is shown in Fig. 3.

In Fig. 3, $S_d(s)$ has a wide notch near $6\omega_e$, making the reduction of disturbance estimation error at $6\omega_e$. However, as $6\omega_e$ increases or ω_0 decreases, the magnitude of $S_d(s)$ in low-frequency range increases, indicating higher observation errors. This behavior can be explained by the Bode Integral Theorem, which $S_d(s)$ satisfies

$$\int_0^\infty \ln\left|\frac{\widetilde{f}_{qz\_total}(j\omega)}{f_{qz\_total}(j\omega)}\right| d\omega = 0. \tag{18}$$

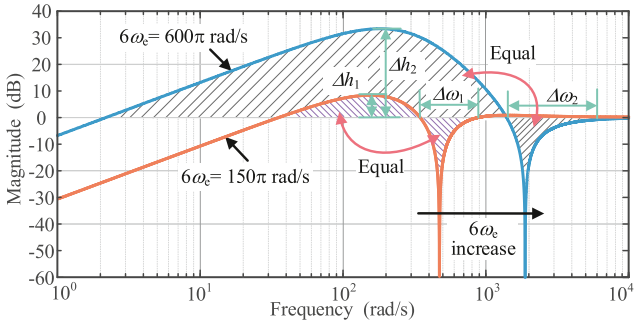

Fig. 4. Magnitude plot of sensitivity function, $\omega_0 = 100\pi$ rad/s.

Equation (18) reflects the waterbed effect, which is that sinking at a certain point will cause an increase in other frequencies. Fig. 4 is carried out to illustrate the effect between the estimation of $\hat{f}_{qz6\omega}$ and $\hat{f}_{qz0}$. With $6\omega_e$ increases, the notch range near $6\omega_e$ will increase, which causes Δh_2 to be greater than Δh_1. Due to the logarithmic scale of frequency, $\Delta\omega_2$ is actually much larger than $\Delta\omega_1$. In addition, the gain l_2 in (15) contains the parameter $6\omega_e$ which is the frequency of periodic disturbance, and the gain l_3 also contains l_2. This also indicates that the observation of $\hat{f}_{qz6\omega}$ and $\hat{f}_{qz0}$ are not independent.

Therefore, following conclusions can be obtained. 1) There is competition between low-frequency disturbance and high-frequency periodic disturbance estimation. The notch range and attenuation of periodic disturbance observations should be limited to improve the estimation of low-frequency disturbances. 2) To reduce the effect between $\hat{f}_{qz6\omega}$ and $\hat{f}_{qz0}$, the observation of $\hat{f}_{qz6\omega}$ and $\hat{f}_{qz0}$ should use the current estimation error within different frequency ranges as inputs, instead of $\widetilde{i}_{qz}(s)$ at full frequency. 3) It is necessary to design the poles of the observer for low-frequency disturbances and high-frequency periodic disturbances, respectively.

C. Proposed IGESO

Based on the above analysis, a more effective disturbance observer structure is proposed in this article, which is designed as

$$\begin{cases} \frac{d}{dt}\hat{i}_{qz} = a_0\hat{i}_{qz} + b_0 u_{qz} + \hat{f}_{qz0} + \hat{f}_{qz6\omega} + l_1\left(i_{qz} - \hat{i}_{qz}\right) \\ \frac{d}{dt}\hat{f}_{qz0} = l_2\left(x_1 + i_{qz} - \hat{i}_{qz}\right) \\ \frac{d}{dt}x_1 = -2\rho_2 x_1 - (6\omega_e)^2 x_2 - 2\rho_2\left(i_{qz} - \hat{i}_{qz}\right) \\ \frac{d}{dt}x_2 = x_1 \\ \frac{d}{dt}\hat{f}_{qz6\omega} = \hat{\gamma} - 2\rho_2\hat{f}_{qz6\omega} + l_3\left(i_{qz} - \hat{i}_{qz}\right) \\ \frac{d}{dt}\hat{\gamma} = -(6\omega_e)^2\hat{f}_{qz6\omega} + l_4\left(i_{qz} - \hat{i}_{qz}\right) \end{cases} \tag{19}$$

where ρ_2 is the damping coefficient, x_1 and x_2 are state variables. Combining (7), the system control block diagram of the proposed IGESO is shown in Fig. 5. $R(s)$ is a notch filter with the center frequency of $6\omega_e$. The relationships between disturbance

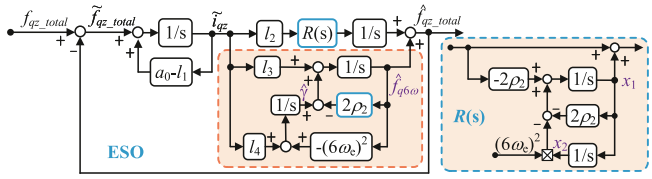

Fig. 5. Block diagram of the q-axis current loop with the IGESO.

observation and $\widetilde{i}_{qz}(s)$ are derived as

$$\begin{cases} \hat{f}_{qz0}(s) = \frac{1}{s} l_2 \frac{s^2+36\omega_e^2}{s^2+2\rho_2 s+36\omega_e^2}\widetilde{i}_{qz}(s) \\ \hat{f}_{qz6\omega}(s) = \frac{sl_3+l_4}{s^2+2\rho_2 s+36\omega_e^2}\widetilde{i}_{qz}(s) \end{cases}. \tag{20}$$

From (20), in the estimation of $\hat{f}_{qz0}$, the input $\widetilde{i}_{qz}(s)$ exhibits a notch at $6\omega_e$, and the notch frequency range is determined by ρ_2. Thus, the current estimation error caused by $\hat{f}_{qz6\omega}$ has little impact on the estimation of $\hat{f}_{qz0}$. Conversely, for the estimation of $\hat{f}_{qz6\omega}$, the input $\widetilde{i}_{qz}(s)$ displays a bandpass at $6\omega_e$, and the pass frequency range is also determined by ρ_2. This achieves input with different frequency ranges.

The characteristic equation of the system is derived as

$$\begin{aligned} \Phi_3(s) = {} & s^4 + (l_1 - a_0 + 2\rho_2)\, s^3 \\ & + \left(36\omega_e^2 + 2(l_1 - a_0)\rho_2 + l_2 + l_3\right) s^2 \\ & + \left((l_1 - a_0)\, 36\omega_e^2 + l_4\right) s + 36\omega_e^2 \cdot l_2. \end{aligned} \tag{21}$$

Compared with placing all four poles at the same location, the characteristic (21) adopts a strategy of four different poles. The poles s_1 and s_2 are fixed and symmetric about the real axis. The other poles s_3 and s_4 vary with ω_e, maintaining a fixed relative position to the zeros to counteract the influence of ω_e. Set the characteristic equation as

$$\Phi_3(s) = \left(s^2 + 2\xi s + \omega_0^2\right)\left(s^2 + 2\rho s + 36\omega_e^2\right) \tag{22}$$

where ξ and ρ are the damping coefficient. Then, the gains of the observer can be obtained as

$$\begin{cases} l_1 = 2\xi\omega_0 + a_0 + 2(\rho - \rho_2) \\ l_2 = \omega_0^2 \\ l_3 = 4\xi\omega_0(\rho - \rho_2) + 4\rho_2(\rho_2 - \rho) \\ l_4 = 2\left(\omega_0^2 - 36\omega_e^2\right)\rho + 36\omega_e^2 \cdot 2\rho_2 \end{cases}. \tag{23}$$

Therefore, the sensitivity function is expressed as

$$\begin{aligned} S_d(s) &= \frac{\widetilde{f}_{qz\_total}(s)}{f_{qz\_total}(s)} \\ &= \underbrace{\frac{s\left(s + 2\xi\omega_0 + 2(\rho - \rho_2)\right)}{\left(s^2 + 2\xi\omega_0 s + \omega_0^2\right)}}_{G_1(s)} \underbrace{\frac{\left(s^2 + 2\rho_2 s + 36\omega_e^2\right)}{\left(s^2 + 2\rho s + 36\omega_e^2\right)}}_{G_2(s)}. \end{aligned} \tag{24}$$

The current estimation error $\widetilde{i}_{qz}(s)$ is derived as

$$\widetilde{i}_{qz}(s) = \frac{s\left(s^2 + 2\rho_2 s + 36\omega_e^2\right)}{\left(s^2 + 2\xi s + \omega_0^2\right)\left(s^2 + 2\rho s + 36\omega_e^2\right)} f_{qz\_\mathrm{total}}(s). \tag{25}$$

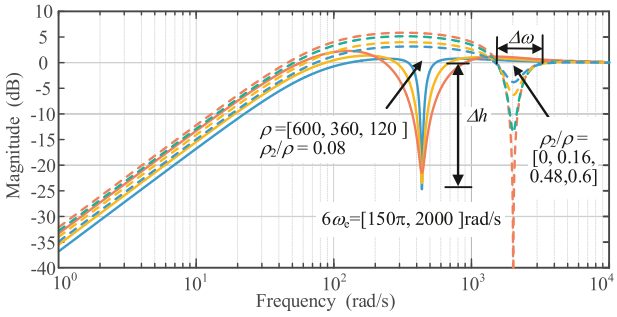

Fig. 6. Magnitude plot of sensitivity function for varying ρ and ρ_2.

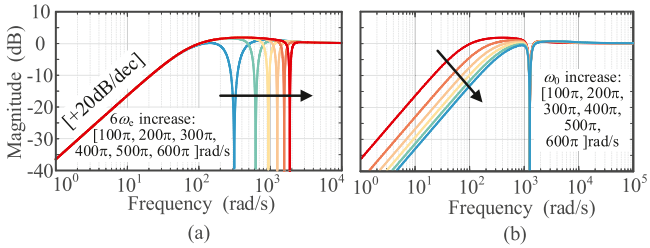

Fig. 7. Magnitude plot of sensitivity function (24). (a) Various $6\omega_e$, $\omega_0 = 100\pi$ rad/s. (b) Various ω_0, $6\omega_e = 400\pi$.

The Magnitude plot of the proposed observer sensitivity function according to (24) is shown in Fig. 6. Compared with Fig. 3, the proposed IGESO has significant improvements. From (24), $G_2(s)$ is a standard notch filter form, which can regulate the notch range and attenuation at the frequency of $6\omega_e$ simultaneously. The notch range is determined by ρ. From the solid lines in Fig. 6, as ρ increases, $\Delta\omega$ becomes larger. Therefore, increasing ρ can enhance robustness against changes in the sixth harmonic frequency and effectively decrease Δh_2. The ratio ρ_2/ρ is related to the attenuation and phase lag at $6\omega_e$. As shown by the dotted lines in Fig. 6, an increase in ρ_2/ρ reduces the magnitude of Δh_2 at the mid-frequencies. Specifically, when $\rho_2 = 0$, it can be attenuated to $-\infty$ at notch frequency. However, in this case, the observer exhibits the largest Δh_2 at mid-frequencies. The Bode plots of various ω_e and ω_0 are shown in Fig. 7. Comparing Fig. 3, it can be seen that IGESO has improved its performance in the mid frequency region.

In addition to considering the amplitude–frequency characteristics, the observer phase should also be considered. According to the sensitivity function (24), the transfer function of the disturbance is expressed as follows:

$$\frac{\hat{f}_{qz\_total}(s)}{f_{qz\_total}(s)} = \frac{f_{qz\_total}(s) - \widetilde{f}_{qz\_total}(s)}{f_{qz\_total}(s)} = 1 - S_d(s). \quad (26)$$

The Bode diagram of the observed disturbance is shown in Fig. 8. The phase approaches 2π at low frequencies and is 0 at $6\omega_e$. The slope of the phase at $6\omega_e$ is primarily determined by ρ and minimally influenced by ρ_2. However, when ω_0 is relatively large, setting $\rho_2 = 0$ will cause the phase to mutate at $6\omega_e$. Modifying ρ allows the regulation of the slope near $6\omega_e$, enhancing the frequency robustness. This adjustment can reduce

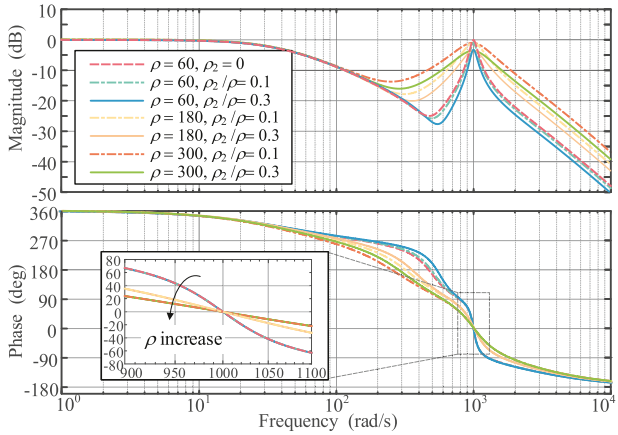

Fig. 8. Bode diagram of disturbance transfer function under various ρ and ρ_2.

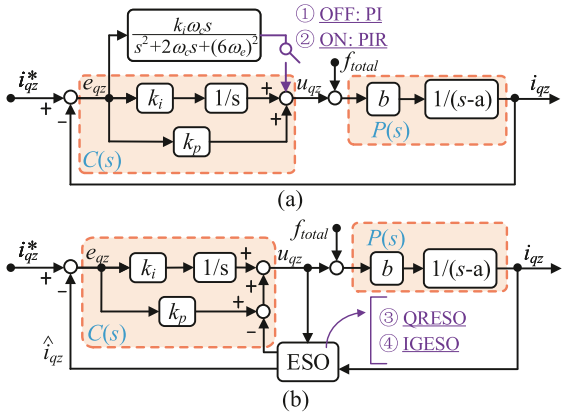

Fig. 9. Close loop in the $dz - qz$ subspace with difference strategies. (a) PI and PIR. (b) QRESO and IGESO.

the observed disturbance's phase lead or lag during frequency disturbance.

D. System Performance Comparison With Other Strategies

To investigate the harmonic suppression strategy based on IGESO further, a close-loop performance comparison with other strategies, in theory, is carried out. Using the PI controller in $dzqz$ current loop, as shown in Fig. 9(a), is the most common method. In [4], a resonant controller is added in parallel called PIR controller to suppress the harmonics of a certain order, as shown in Fig. 9(a). In addition, QRESO, which has gained attention in recent years, is also included in this comparison. QRESO can observe the periodic disturbances by adding a resonant term to the traditional ESO method [28]. The closed-loop control block diagrams for QRESO and IGESO are shown in Fig. 9(b).

In fact, QRESO can be viewed as a specific case of GESO. It only needs to set the observer gains of (13) to

$$\begin{cases} l_1 = \beta_1 \\ l_2 = \beta_2 \\ l_3 = 0 \\ l_4 = 2\beta_2 k_r \omega_c \end{cases}. \quad (27)$$

TABLE I
COMPARISON RESULTS OF DIFFERENT STRATEGIES IN $dz-Qz$ SUBSPACE

Item	① PI	② PIR	③ PI+QRESO	④ PI+IGESO
Plant	$P(s)=b/(s-a)$			
Controller	$C(s)=k_p+k_i/s$			
Auxiliary function	-	$R(s)=\frac{k_r\omega_c s}{s^2+2\omega_c s+(6\omega_e)^2}$	$F_1(s)=\frac{\tilde{f}_{qz\_total}}{f_{qz\_total}}=\frac{s(s+\beta_1)}{s(s+\beta_1)+\beta_2+\beta_2 R(s)}$ $F_2(s)=\frac{\tilde{i}_{qz}}{f_{qz\_total}}=\frac{F_1(s)}{s-a_0+\beta_1}$	$F_1(s)=\frac{\tilde{f}_{qz\_total}}{f_{qz\_total}}=Eq.(24)$ $F_2(s)=\frac{\tilde{i}_{qz}}{f_{qz\_total}}=\frac{F_1(s)}{s-a_0+l_1}$
$\frac{i_{qz}(s)}{i^*_{qz}(s)}$	$\frac{C(s)P(s)}{1+C(s)P(s)}$	$\frac{[C(s)+R(s)]P(s)}{1+[C(s)+R(s)]P(s)}$	$\frac{C(s)P(s)}{1+C(s)P(s)}$	
$\frac{i_{qz}(s)}{f_{qz\_total}(s)}$	$\frac{P(s)}{1+C(s)P(s)}$	$\frac{P(s)}{1+[C(s)+R(s)]P(s)}$	$\frac{C(s)P(s)}{1+C(s)P(s)}F_2(s)+\frac{P(s)}{1+C(s)P(s)}F_1(s)$	

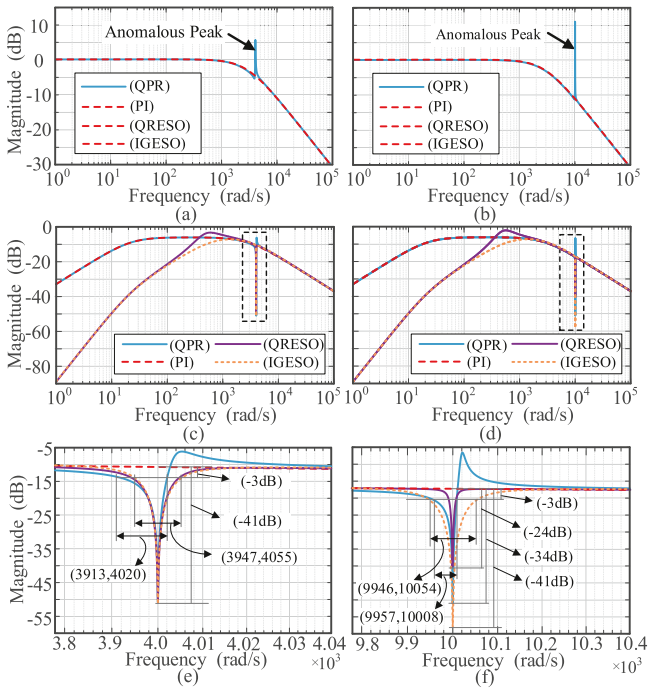

Fig. 10. Close-loop frequency-response diagram of $dz-qz$ current loop for four strategies. (a) and (b) Tracking performance. (c) and (d) Disturbance suppression performance. (e) and (f) Zoomed view of (c) and (d). (a), (c), and (e) at frequency 4000 rd/s. (b), (d), and (f) at frequency 10000 rd/s.

The observed disturbance of QRESO is expressed as

$$\hat{f}_{qz\_\text{total}}(s)=\frac{\beta_2}{s}\left[1+\frac{2k_r\omega_c s}{s^2+2\omega_c s+(6\omega_e{}^2)}\right]\tilde{i}_{qz}(s)$$
$$=\frac{\beta_2}{s}\left[1+R(s)\right]\tilde{i}_{qz}(s). \quad (28)$$

The four strategies exhibit different performances in disturbance suppression and reference tracking, with their transfer functions given in Table I. The table's third row and fourth reflects tracking and anti-disturbance performance, respectively. Fig. 10 displays the close-loop frequency-response of each strategy, with parameters adjusted for fair comparison. All strategies use the same k_p and k_i. In the PIR, QRESO and IGESO methods, which can suppress the periodic disturbance, the parameters are fine-tuned to align the same notch frequency range and attenuation at the disturbance frequency (4000 rd/s). In addition, QRESO and IGESO maintain a consistent attenuation at low frequencies.

According to Fig. 10, all methods provide disturbance suppression, with performance differences focused on suppression range and frequency sensitivity. Fig. 10(c) and (d) shows that PIR, QRESO, and IGESO improve periodic disturbance suppression over PI. Furthermore, QRESO and IGESO also enhance low-frequency disturbance suppression, more effectively addressing the lumped disturbance in (9). However, QRESO shows some deterioration in the mid-frequency region.

As shown in Fig. 10(e), the frequency range of PIR is asymmetric around the center frequency, indicating worse frequency sensitivity. Furthermore, as disturbance frequency increases, the frequency suppression range narrows for both PIR and QRESO, with a decrease in attenuation and frequency sensitivity, as shown in Fig. 10(f). Therefore, regulating higher frequency harmonics with the PIR or QRESO becomes a challenge. The proposed IGESO method can provide the same suppression range and attenuation across frequencies.

In reference tracking, the resonant term in the PIR not only suppresses harmonics, but also enables tracking of the sinusoidal signal. However, at higher frequencies, the PIR produces anomalous peaks greater than 0dB near the resonant frequency, as shown in Fig. 10(a) and (b). These peaks indicate an amplification of relevant frequency components, which can degrade system dynamics, cause overshoot, and increase noise. QRESO and IGESO, designed with a 2DOF control structure, provide the same tracking performance as PI. According to the third row of Table I, the design of the observer will not affect the tracking performance of the system. This allows for independent design and optimization of tracking and disturbance suppression.

From the analysis above, compared with other strategies, the system with IGESO has a better tracking performance and disturbance suppression ability in the whole working frequency without causing system degradation, which proves the advantages of IGESO in theory.

IV. STABILITY ANALYSIS

A. Observer Stability Analysis

To digitally implement the proposed IGESO, its discrete expression is required. From (19) and Fig. 5, the implementations of $\hat{f}_{qz6\omega}$ and $\hat{f}_{qz0}$ in IGESO both need two integrators. The

direct integrator is discretized with the forward Euler method, while the feedback uses the backward Euler method [34]. Thus, the discrete expression of IGESO can be derived as follows: By selecting appropriate observer parameters according to (23), the total disturbance of the system and the current on the dz–qz axis can be accurately estimated.

The stability of discrete IGESO depends on the eigenvalues of the characteristic polynomial. Discrete IGESO is stable when all eigenvalues are within the z-plane unit circle. For (29) shown at the bottom of this page, its characteristic polynomial is

$$G(z) = z^4 + n_1 z^3 + n_2 z^2 + n_3 z + n_4 \tag{31}$$

where n_1, n_2, n_3, and n_4 are shown in (30) shown at the bottom of this page.

According to [34], a accurate resonant frequency can be obtained by using the Taylor expansion of $2[1-\cos(6\omega_e T_s)]/T_s^2$ instead of $6\omega_e$. The first two terms of the expansion is taken in this article, that is

$$\omega_h^2 = (6\omega_e)^2 - \frac{(6\omega_e)^4 T_s^2}{12} \tag{32}$$

where ω_h is the resonant frequency. The pole diagram of IGESO is shown in Fig. 11. It can be seen that all the poles of observer are within the unit circle of the z plane.

To further analyze the impact of parameters variations on the observer stability, the pole distribution of discrete IGESO with changes in parameters ρ, ξ, and $6\omega_e$ is given, as shown in Fig. 11.

From the dotted trajectory of poles p_3 and p_4 in Fig. 11, the resonant frequency has only minor error as $6\omega_e$ increases due to frequency correction by (32). As ρ increases, p_3 and p_4 move away from the unit circle, as indicated by the solid trajectories in Fig. 11. The pole p_2 will move toward the center of the circle as ξ increases and another pole p_1 is located at (1,0). All poles remain within the unit circle as parameters change, confirming that the discretized system is stable under the parameter tuning method proposed in this article.

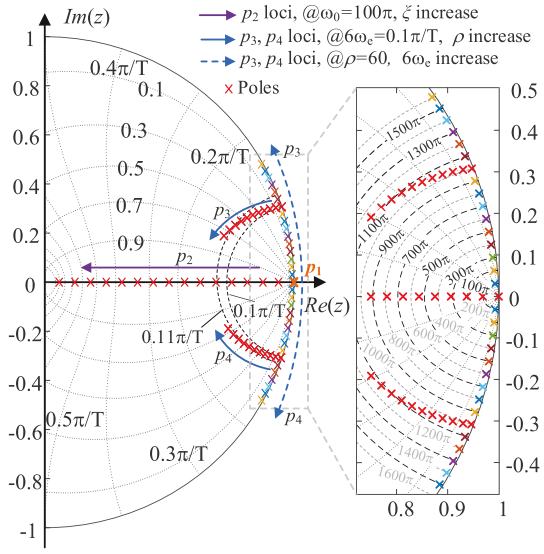

Fig. 11. Pole analysis of IGESO.

B. Stability Analysis of Closed Loop Systems

According to Fig. 9(b), the discretized current loop model including IGESO is expressed as

$$\begin{cases} u_{qz}(k+1) = -\frac{1}{b_0}\hat{f}_{qz\_total}(k+1) - k_p\left[i_{qz}^*(k) - \hat{i}_{qz}(k)\right] \\ +\left[k_p + T_s * k_i\right]\left[i_{qz}^*(k+1) - \hat{i}_{qz}(k+1)\right] + u_{qz}(k) \\ i_{qz}(k+2) = i_{qz}(k+1) + T_s a_0 i_{qz}(k+1) \\ +T_s b_0 u_{qz}(k+1) + T_s f_{qz\_\mathrm{total}}(k+1) \end{cases}. \tag{33}$$

Same as the observer stability, when all eigenvalues are within the unit circle of the z-plane, the current closed-loop control system is stable. For the system composed of (33) and (29), its characteristic polynomial can be expressed as

$$G_{\mathrm{cl}}(z) = [z^2 + \left(T_s{}^2 k_i - T_s a_0 + T_s k_p - 2\right) z + T_s a_0 - T_s k_p + 1] G(z). \tag{34}$$

$$\begin{cases} \hat{i}_{qz}(k+1) = (1 + a_0 T_s)\hat{i}_{qz}(k) + b_0 T_s u_{qz}(k) + T_s\left[\hat{f}_{qz0}(k) + \hat{f}_{qz6\omega}(k)\right] + l_1 T_s\left[i_{qz}^m(k) - \hat{i}_{qz}(k)\right] \\ \hat{f}_{qz0}(k+1) = \hat{f}_{qz0}(k) + T_s l_2\left[x_1(k) + i_{qz}^m(k) - \hat{i}_{qz}(k)\right] \\ x_1(k+1) = x_1(k) - 2\rho_2 T_s\left[i_{qz}^m(k) - \hat{i}_{qz}(k)\right] - T_s\left[(6\omega_e)^2 x_2(k) + 2\rho_2 x_1(k)\right] \\ x_2(k) = x_2(k-1) + T_s x_1(k) \\ \hat{f}_{qz6\omega}(k+1) = \hat{f}_{qz6\omega}(k) + T_s l_3\left[i_{qz}^m(k) - \hat{i}_{qz}(k)\right] + T_s\left[\hat{\gamma}(k) - 2\rho_2 \hat{f}_{qz6\omega}(k)\right] \\ \hat{\gamma}(k) = \hat{\gamma}(k-1) + T_s\left[(6\omega_e)^2 \hat{f}_{qz6\omega}(k)\right] + T_s l_4\left[i_{qz}^m(k) - \hat{i}_{qz}(k)\right] \end{cases} \tag{29}$$

$$\begin{cases} n_1 = \left[(6\omega_e)^2 + l_2\right] T_s^2 + (l_1 - a_0 + 2\rho_2) T_s - 4 \\ n_2 = \left[(l_1 - a_0)(6\omega_e)^2 + l_4\right] T_s^3 + (3a_0 - 3l_1 - 6\rho_2) T_s + \left[2(l_1 - a_0)\rho_2 - 2(6\omega_e)^2 - 2l_2 + l_3\right] Ts^2 + 6 \\ n_3 = -4 + \left[(a_0 - l_1)(6\omega_e)^2 - l_4\right] T_s^3 + \left[(6\omega_e)^2 + 4(a0 - l_1)\rho_2 + l_2 - 2l_3\right] T_s^2 + (-3a_0 + 3l_1 + 6\rho_2) T_s \\ n_4 = 1 + [2(l_1 - a_0)\rho_2 + l_3] Ts^2 + (a_0 - l_1 - 2\rho_2) T_s \end{cases}. \tag{30}$$

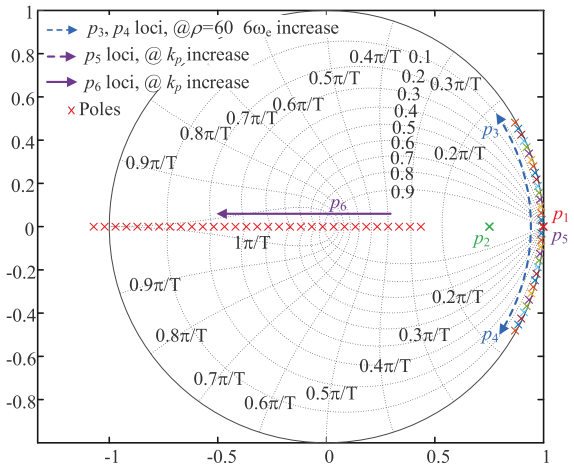

Fig. 12. Pole analysis of $G_{cl}(z)$.

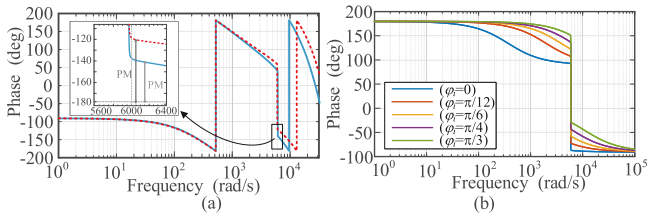

Fig. 13. Open-loop Bode diagrams. (a) The plant is included. (b) The plant is not included with different φ_i values. Parameters: $\omega_h = 1900\pi$.

Taking the parameters ($T_s = 1/10000$s, $\xi = 4$, $\rho = 60$, $\rho_2 = 6$, $\omega_0 = 100\pi$), the eigenvalue location of (34) is shown in Fig. 12. Two additional poles, p_5 and p_6, are included compared to (31), as indicated in (34). To analyze the effect of various current loop gains (k_p) on the stability of the current loop control, p_5 and p_6 distribution changes with k_p (ranging from 5000 to 20 000), while other parameters remain constant, as shown in Fig. 12. As k_p increases, p_6 will move outside the unit circle along the real axis. p_5 always located near the position $(1, 0)$. If the value of k_p exceeds $2/T_s + a_0$, pole p_6 will locate outside the unit circle, that is, the closed-loop control system is unstable, assuming that $T_s^2 k_i$ is very small.

C. Observer Phase Margin Compensation

The phase margin of observer decreases when the disturbance frequency is high, multiple IGESOs are present, or there is system delay. Therefore, it is necessary to introduce a phase lead φ_{ω_h} in the vicinity of the frequency ω_h. $\hat{f}_{qz6\omega}$ with phase compensation is expressed as

$$\hat{f}_{qz6\omega}(s) = \frac{l_3\left[s\cos(\varphi_{\omega_h}) - \omega_h \sin(\varphi_{\omega_h})\right] + l_4}{s^2 + 2\rho_2 s + \omega_h^2} \tilde{i}_{qz}(s). \quad (35)$$

For different values of φ_{ω_h}, it can be appreciated the variation of phase lead introduced in Fig. 13(b). In this manner, the open-loop transfer function according to Fig. 5 can permit to improvement of stability of observer. The open-loop transfer function before and after phase compensation ($\varphi_{\omega_h} = pi/3$) are shown in Fig. 13, and the phase margin with compensation is significantly increased.

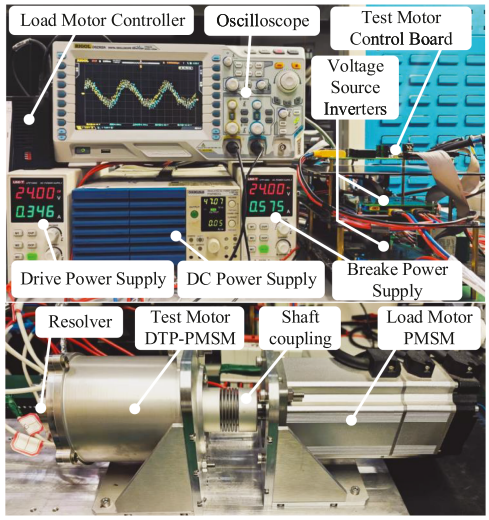

Fig. 14. Experimental setup.

TABLE II
PARAMETERS OF THE TESTED DTP-PMSM

Quantity	Value	Quantity	Value
Rated power P_N	750(W)	Stator resistance R_s	32.7(mΩ)
Rated voltage U_N	48(V)	d axis inductance L_d	184.4(μH)
Rated current I_N	15(A)	q axis inductance L_q	184.4(μH)
Rated speed n_N	1200(rpm)	dz axis inductanceL_{dz}	32.1(μH)
Rated torque T_N	5(Nm)	qz axis inductanceL_{qz}	32.1(μH)
Number of poles p	5	Flux linkage ψ_{PM}	0.0114(Wb)

V. Experimental Verification

To verify the feasibility and validity of IGESO, several experiments are carried out on a laboratory DTP-PMSM system using a DSP TMS320F28375D controller. The experiment setup is shown in Fig. 14, and the parameters of the tested DTP-PMSM are given in Table II. The control and sample frequency is set to 10 kHz. Another PMSM is used as a load motor connected to the tested DTP-PMSM by a shaft coupling. In the following results, experimental data are outputted to the oscilloscope by the integrated DAC module of the microcontroller at a rate of one data frame per 100 μs. In order to verify the improved performance of proposed IGESO, the experimental results of no harmonic current control, The PID control with ESO method [23], [33], PIR control, and PI control with QRESO [28] have also been presented as a benchmark for comparison. In dz–qz subspace, the dz-axis and qz-axis reference current are kept as 0. In the ESO method, the observer is designed as (11). Other methods are shown in Table I and Fig. 9.

A. Steady-State Performance

First, to verify the importance of the control in dz–qz subspace, the phase currents without observer under various operating conditions are shown. Then, the waveforms of phase A and

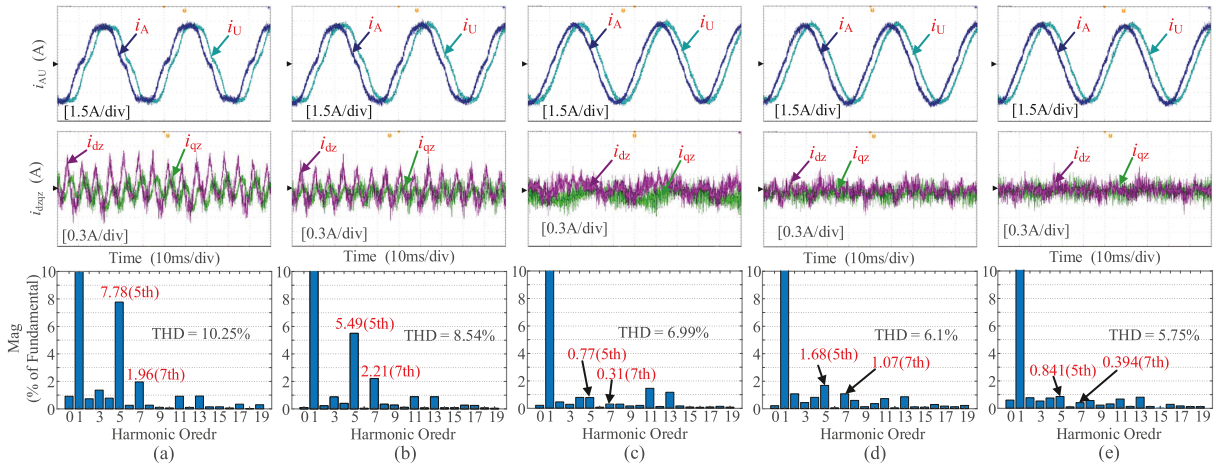

Fig. 15. Experimental results of stator currents, dz–qz axes currents and THD in low-speed light load condition. (a) PI control. (b) Traditional ESO. (c) PIR with $k_r = 950\pi$. (d) QRESO with $\omega_0 = 600\pi$. (e) The Proposed IGESO with $\omega_0 = 400\pi$.

TABLE III
RMS VALUES OF PHASE CURRENTS

Condition	PI	ESO	PIR	QRESO	IGESO
300 rpm, 3.75 A	2.884 A	2.881 A	2.876 A	2.874 A	2.872 A
300 rpm, 15 A	10.8378 A	10.780 A	10.75 A	10.741 A	10.735 A
1200 rpm, 3.75 A	3.188 A	3.187 A	3.175 A	3.179 A	3.174 A
1200 rpm, 15 A	10.797 A	10.790 A	10.742 A	10.782 A	10.736 A

U currents, dz–qz axes currents, and total harmonic distortion (THD) analysis of phase A current under various strategies are shown in Figs. 15– 18. Experiments are implemented under four different operating conditions: low-speed light load (300 r/min, 3.75 A), low-speed rated load (300 r/min, 15 A), rated-speed light load (1200 r/min, 3.75 A), and rated-speed rated load (1200 r/min, 15 A). Finally, to demonstrate the improvement in system efficiency by harmonic suppression, the root mean square (rms) values of the phase currents are calculated, as shown in Table III.

From Figs. 15 and 17, although the reference voltage is 0, there are obvious current harmonics in the phase currents. The harmonic currents in the dz–qz subspace are six times the frequency of the phase current. As analyzed in Section II, the phase current of DTP-PMSM has more current harmonics compared to that of a PMSM. Current harmonics are mainly mapped in the dz–qz subspace as the sixth harmonic. The peak-to-peak of i_{dz} is up to 1.4 A without harmonic current control. And the peak-to-peak current with ESO, PIR, QRESO and IGESO are 1.1 A, 0.8, 0.8 A and 0.6 A, respectively. The proposed IGESO method is better than others. This can also be obtained from the THD of the phase current. The fifth- and seventh-order harmonics of IGESO are the smallest, and the THD is also the smallest.

The PIR method, QRESO, and IGESO has similar performance at sixth order harmonic suppression, because they have been optimized for the sixth harmonic. However, the PIR method exhibits obvious low-frequency harmonics in i_{dz} and i_{qz}. As

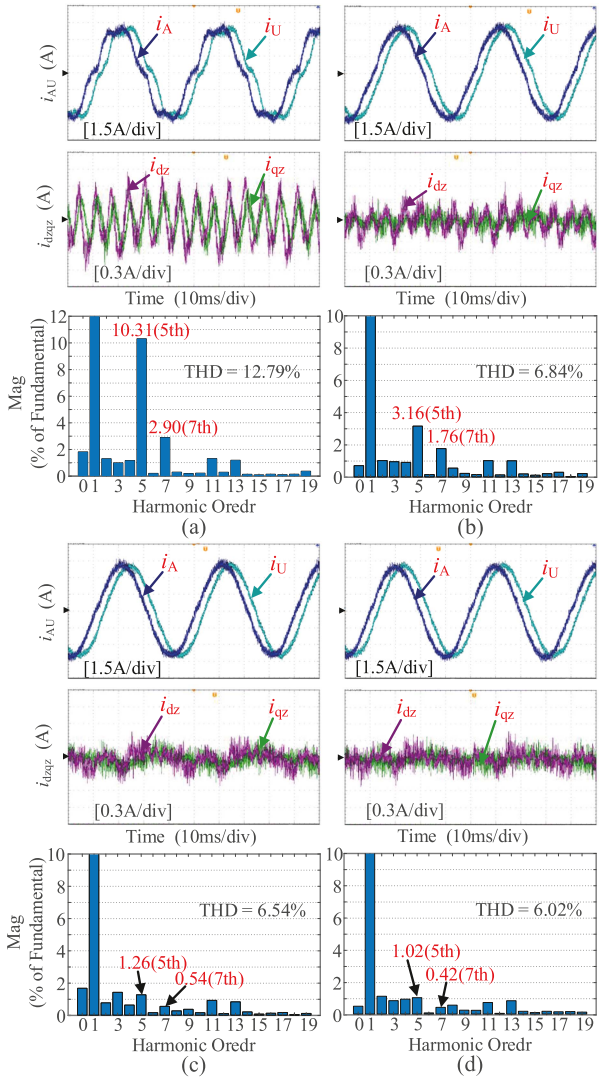

Fig. 16. Experimental results of currents under various ω_0. (a) QRESO with $\omega_0 = 100\pi$. (b) QRESO with $\omega_0 = 300\pi$. (c) IGESO with $\omega_0 = 100\pi$. (d) IGESO with $\omega_0 = 300\pi$.

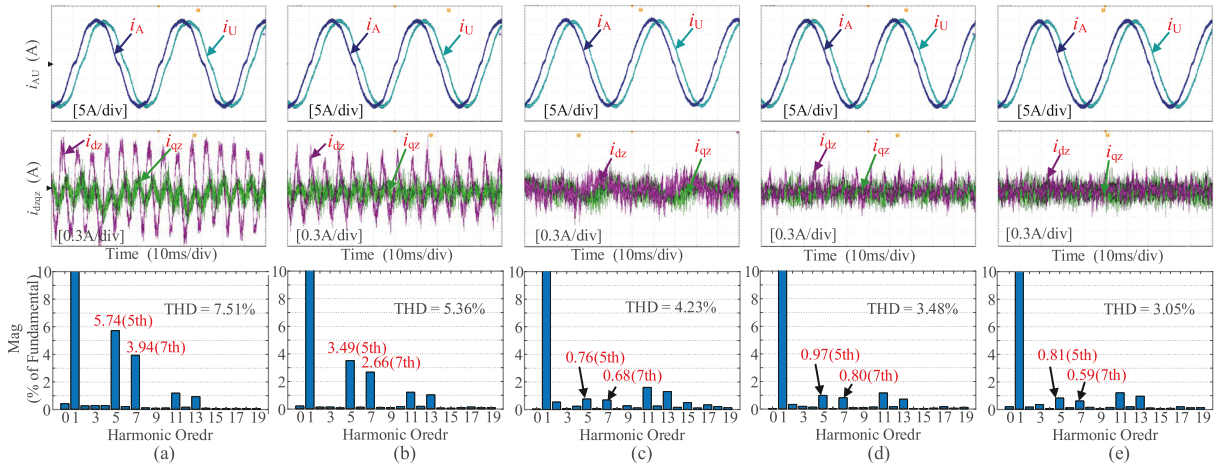

Fig. 17. Experimental results of stator currents, dz-qz axes currents and THD in low-speed rated load condition. (a) PI control. (b) Traditional ESO. (c) PIR. (d) QRESO. (e) The Proposed IGESO.

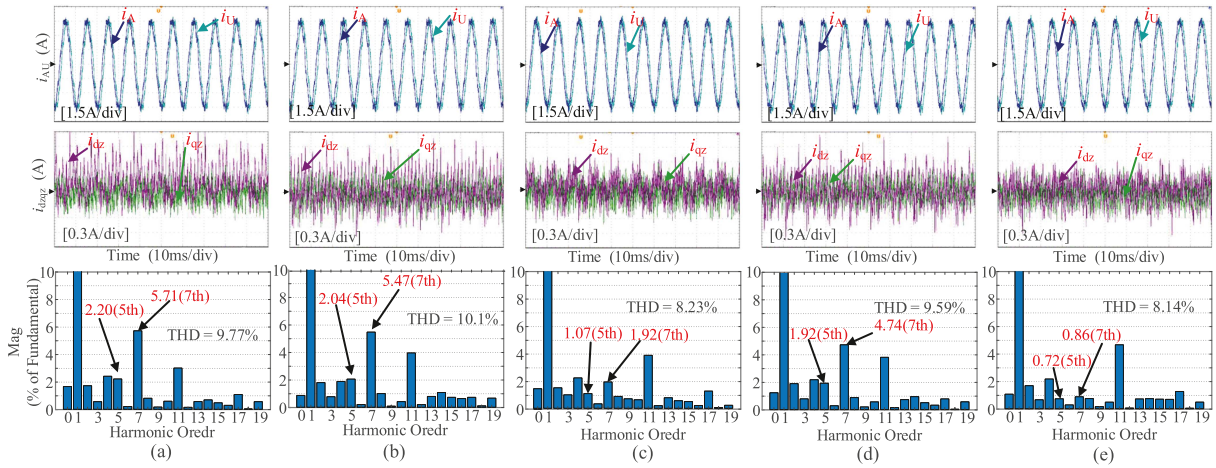

Fig. 18. Experimental results of stator currents, dz-qz axes currents and THD in rated-speed light load condition. (a) PI control. (b) Traditional ESO. (c) PIR. (d) QRESO. (e) The Proposed IGESO.

analyzed in Section III-D, the PIR method does not offer additional suppression for low-frequency disturbances. QRESO method is affected by ω_0. ω_0 is the parameter for low-frequency disturbances, and a larger ω_0 will amplify the noise. As shown in Fig. 16(a), when ω_0 is 100π, the disturbance is not suppressed but amplified. It is consistent with the analysis in Section III. The suppression of low-frequency disturbances will affect the suppression of the sixth harmonic. The suppression performance will be better with the increase of ω_0, as shown in Figs. 15(d), 16(a) and (b). However, the sixth harmonic suppression effect of IGESO method is not affected by the change of ω_0, as shown in Figs. 15(d), 16(c) and (d). Therefore, the proposed IGESO method can operate at a lower ω_0.

Similar conclusions can be drawn at high rotor speeds, as shown in Figs. 18 and 19. The performance of IGESO is still better than that of other strategies. Compared to harmonic currents at low speed, the harmonic currents at high speed are more complicated. However, the THD is not very large. It is because at high speeds, the pulsewidth modulation (PWM) duty ratio is relatively large and the impact of harmonic voltage is reduced. Therefore, the performance improvement of harmonic suppression algorithm is no longer particularly significant. However, IGESO still performs best.

From Table III, all three methods can reduce rms and improve system efficiency. The rms of proposed IGESO is the smallest under various operating conditions. Therefore, its efficiency is the highest.

B. Transient-State Performance

Fig. 20 shows the experimental results of speed step response when the rotor speed steps from 200 to 1000 r/min. The maximum acceleration is 4000 r/min/s. The i_q current and speed response of the two methods are almost the same. It is mainly because the currents in the dz–qz subspace can not affect the dq subspace. The proposed observer is stable at the moment of acceleration and can quickly suppress harmonic currents. Similar conclusions can be drawn from the speed ramp response,

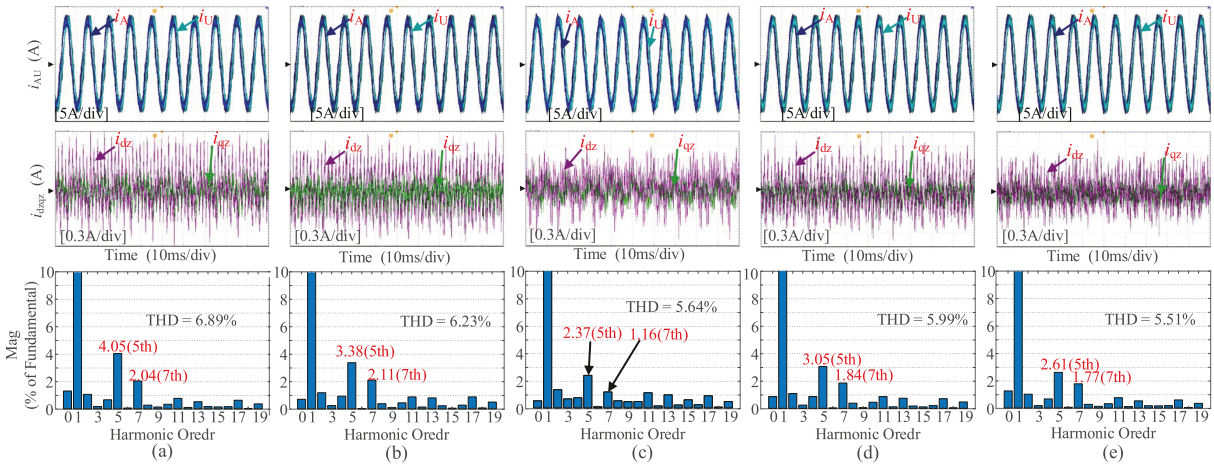

Fig. 19. Experimental results of stator currents, dz–qz axes currents and THD in rated-speed rated load condition. (a) PI control. (b) Traditional ESO. (c) PIR. (d) QRESO. (e) The Proposed IGESO.

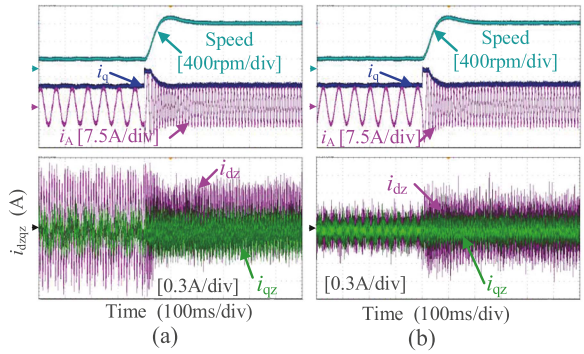

Fig. 20. Speed steps response, from 200 to 1000 r/min. (a) No harmonic current control. (b) The Proposed IGESO.

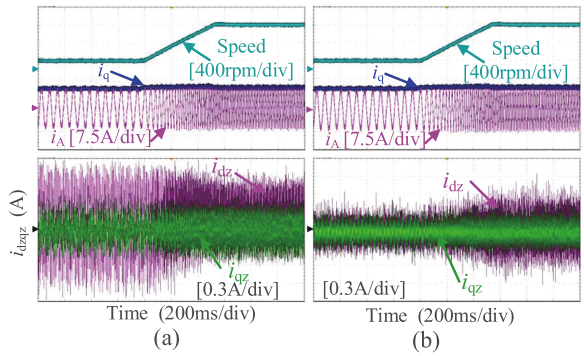

Fig. 21. Speed ramp response, from 200 to 1000 r/min. (a) No harmonic current control. (b) The Proposed IGESO.

as shown in Fig. 21. The acceleration is 1000 r/min/s. The current fluctuations with the proposed IGESO remain low. It verifies the transient performance as well as the harmonic disturbance rejection ability of the proposed IGESO under varying speeds.

As shown in Fig. 22, when the system experiences a sudden increase in load, the IGESO method responds more quickly, maintaining i_{dz} and i_{qz} at consistently low harmonic levels.

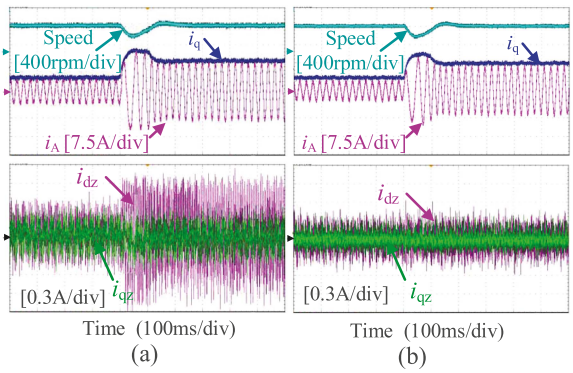

Fig. 22. The load changes from 20% to 70% of the rated load, speed 400 r/min. (a) No harmonic current control. (b) The Proposed IGESO.

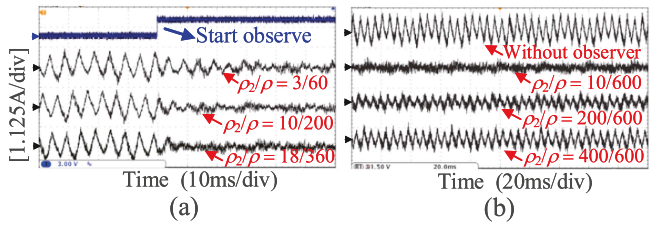

Fig. 23. Effect of parameter changes on observer performance. (a) ρ_2/ρ remain unchanged, increase ρ. (b) ρ remain unchanged, increase ρ_2.

Parameters ρ and ρ_2 have a significant impact on the suppression of sixth harmonic. Fig. 23(a) demonstrates the effect of the parameters ρ on the observer convergence speed. It takes about 20 ms for $\rho = 60$ to settle down and less time for $\rho = 200$ and $\rho = 360$, 10 ms and 7 ms respectively. It is because parameter ρ mainly affects the notch range, so the convergence speed of the observer is closely related to parameter ρ. Fig. 23(b) shows the effect of ratio ρ_2/ρ on the attenuation of the sixth harmonic. A lower ρ_2/ρ will enhance the suppressing sixth harmonic

TABLE IV
CONVERGENCE TIME AND EXCUTION TIME UNDER 300 R/MIN, 25% RATED LOAD

Item	ESO	PIR	QRESO	IGESO
Convergence time(ms)	10	30	110	20
Execution time(μs)	39.6	41	40.8	43.2

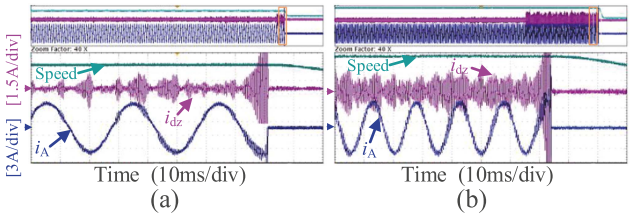

Fig. 24. Stability analysis with k_p increase. (a) 400r/min. (b) 800 r/min.

disturbances. When ρ_2/ρ is 2/3, an obvious sixth harmonic can be seen.

The convergence speed of the IGESO compared to other strategies is presented in Table IV. The convergence speed of IGESO is not the fastest among all methods, but it is significantly faster than QRESO. Considering the overall suppression performance, the convergence speed of IGESO is acceptable.

The execution time of IGESO in the interrupt is the longest among all methods. However, the increase in computation time is justified by the improvements in harmonic suppression performance and does not adversely affect the real-time performance of the controller.

C. Closed Loop System Stability Experiments

As shown in Fig. 24, the given parameter of the gain k_p of dz- and qz-axis current controller changes from $1.4a_0$ to a_0 with the rotor speed of 400 and 800 r/min. Continuing to increase k_p will cause the motor to fall out of synchronism, and the phase current will overcurrent. It is demonstrated that the stability of the current loop is determined by the parameter k_p.

VI. CONCLUSION

The IGESO method is proposed to suppress the harmonic currents of the DTP-PMSM. This article covers the working principle of IGESO, performance analysis, parameter design principles, and the stability range of the current closed-loop system including the IGESO. Experimental results have been presented to verify the effectiveness of the proposed method. The following contributions was achieved.

1) Effective suppression of current harmonics can be achieved over the entire speed range.
2) The parameters of the observer's low-frequency disturbance and periodic disturbance are designed separately. The observer can operate with a bandwidth much lower than other observers.
3) The influence of observer parameters on harmonic suppression performance is analyzed in detail, and parameter design principles are provided.
4) The stability analysis of IGESO and the entire current closed-loop control system in the discrete time domain is given. Experiments are conducted to compare with other observers to prove the effectiveness and superiority of IGESO.

In addition, this method is an optimization of the traditional harmonic control method and can be applied to other disturbance suppression with known disturbance frequencies. It can not only suppress current harmonics, but also speed harmonics and torque pulsation.

REFERENCES

[1] E. Levi, "Multiphase electric machines for variable-speed applications," *IEEE Trans. Ind. Electron.*, vol. 55, no. 5, pp. 1893–1909, May 2008.
[2] J. Karttunen, S. Kallio, P. Peltoniemi, P. Silventoinen, and O. Pyrhönen, "Decoupled vector control scheme for dual three-phase permanent magnet synchronous machines," *IEEE Trans. Ind. Electron.*, vol. 61, no. 5, pp. 2185–2196, May 2014.
[3] J. K. Pandit, M. V. Aware, R. V. Nemade, and E. Levi, "Direct torque control scheme for a six-phase induction motor with reduced torque ripple," *IEEE Trans. Power Electron.*, vol. 32, no. 9, pp. 7118–7129, Sep. 2017.
[4] Y. Hu, Z. -Q. Zhu, and K. Liu, "Current control for dual three-phase permanent magnet synchronous motors accounting for current unbalance and harmonics," *IEEE J. Emerg. Sel. Topics Power Electron.*, vol. 2, no. 2, pp. 272–284, Jun. 2014.
[5] H. M. Eldeeb, A. S. Abdel-Khalik, and C. M. Hackl, "Dynamic modeling of dual three-phase IPMSM drives with different neutral configurations," *IEEE Trans. Ind. Electron.*, vol. 66, no. 1, pp. 141–151, Jan. 2019.
[6] Y. Zhao and T. A. Lipo, "Space vector PWM control of dual three-phase induction machine using vector space decomposition," *IEEE Trans. Ind. Appl.*, vol. 31, no. 5, pp. 1100–1109, Sep./Oct. 1995.
[7] B. Zheng, J. Zou, Y. Xu, G. Yu, L. Wang, and P. Zanchetta, "High-frequency current harmonic analysis and suppression in dual three-phase PMSMs with advanced carrier phase-shift PWM," *IEEE Trans. Power Electron.*, vol. 39, no. 2, pp. 2569–2581, Feb. 2024.
[8] C. Zhou, G. Yang, and J. Su, "PWM strategy with minimum harmonic distortion for dual three-phase permanent-magnet synchronous motor drives operating in the overmodulation region," *IEEE Trans. Power Electron.*, vol. 31, no. 2, pp. 1367–1380, Feb. 2016.
[9] J. -H. She, M. Fang, Y. Ohyama, H. Hashimoto, and M. Wu, "Improving disturbance-rejection performance based on an equivalent-input-disturbance approach," *IEEE Trans. Ind. Electron.*, vol. 55, no. 1, pp. 380–389, Jan. 2008.
[10] J. Karttunen, S. Kallio, P. Peltoniemi, and P. Silventoinen, "Current harmonic compensation in dual three-phase PMSMs using a disturbance observer," *IEEE Trans. Ind. Electron.*, vol. 63, no. 1, pp. 583–594, Jan. 2016.
[11] Y. Luo, K. Yang, and Y. Zheng, "Luenberger observer-based model predictive control for six-phase PMSM motor with localization error compensation," *IEEE Trans. Ind. Electron.*, vol. 70, no. 11, pp. 10800–10810, Nov. 2023.
[12] O. Gonzalez, M. Ayala, C. Romero, L. Delorme, and J. Rodas, "Model predictive current control of six-phase induction motor drives using virtual vectors and space vector modulation," *IEEE Trans. Power Electron.*, vol. 37, no. 7, pp. 7617–7628, Jul. 2022.
[13] I. Gonzalez-Prieto, M. J. Duran, J. J. Aciego, C. Martin, and F. Barrero, "Model predictive control of six-phase induction motor drives using virtual voltage vectors," *IEEE Trans. Ind. Electron.*, vol. 65, no. 1, pp. 27–37, Jan. 2018.
[14] M. Ayala, J. Doval-Gandoy, J. Rodas, O. Gonzalez, R. Gregor, and M. Rivera, "A novel modulated model predictive control applied to six-phase induction motor drives," *IEEE Trans. Ind. Electron.*, vol. 68, no. 5, pp. 3672–3682, May 2021.
[15] J. J. Aciego, I. González Prieto, M. J. Duran, M. Bermudez, and P. Salas-Biedma, "Model predictive control based on dynamic voltage vectors for six-phase induction machines," *IEEE J. Emerg. Sel. Topics Power Electron.*, vol. 9, no. 3, pp. 2710–2722, Jun. 2021.
[16] W. Wang, C. Liu, Z. Song, and Z. Dong, "Harmonic current suppression for dual three-phase PMSM based on deadbeat control and disturbance observer," *IEEE Trans. Ind. Electron.*, vol. 70, no. 4, pp. 3482–3492, Apr. 2023.

[17] H. Yi, F. Zhuo, and F. Wang, "Analysis about overshoot peaks appearing in the current loop with resonant controller," *IEEE J. Emerg. Sel. Topics Power Electron.*, vol. 4, no. 1, pp. 26–36, Mar. 2016.
[18] J. Karttunen, S. Kallio, J. Honkanen, P. Peltoniemi, and P. Silventoinen, "Partial current harmonic compensation in dual three-phase PMSMs considering the limited available voltage," *IEEE Trans. Ind. Electron.*, vol. 64, no. 2, pp. 1038–1048, Feb. 2017.
[19] L. Yan, Z. Zhu, J. Qi, Y. Ren, and C. Gan, "Suppression of major current harmonics for dual three-phase PMSMs by virtual multi three-phase systems," *IEEE Trans. Ind. Electron.*, vol. 69, no. 6, pp. 5478–5490, Jun. 2022.
[20] W. Chen, J. Yang, L. Guo, and S. Li, "Disturbance-observer-Based control and related methods-an overview," *IEEE Trans. Ind. Electron.*, vol. 63, no. 2, pp. 1083–1095, Feb. 2016.
[21] O. Babayomi and Z. Zhang, "Model-free predictive control of power converters with multifrequency extended state observers," *IEEE Trans. Ind. Electron.*, vol. 70, no. 11, pp. 11379–11389, Nov. 2023.
[22] J. Han, "From PID to active disturbance rejection control," *IEEE Trans. Ind. Electron.*, vol. 56, no. 3, pp. 900–906, Mar. 2009.
[23] Y. Xu, B. Zheng, G. Wang, H. Yan, and J. Zou, "Current harmonic suppression in dual three-phase permanent magnet synchronous machine with extended state observer," *IEEE Trans. Power Electron.*, vol. 35, no. 11, pp. 12166–12180, Nov. 2020.
[24] K. -S. Kim, K.-H. Rew, and S. Kim, "Disturbance observer for estimating higher order disturbances in time series expansion," *IEEE Trans. Autom. Control.*, vol. 55, no. 8, pp. 1905–1911, Aug. 2010.
[25] A. A. Godbole, J. P. Kolhe, and S. E. Talole, "Performance analysis of generalized extended state observer in tackling sinusoidal disturbances," *IEEE Trans. Control Syst. Technol.*, vol. 21, no. 6, pp. 2212–2223, Nov. 2013.
[26] Y. Zuo, J. Chen, X. Zhu, and C. H. T. Lee, "Different active disturbance rejection controllers based on the same order GPI observer," *IEEE Trans. Ind. Electron.*, vol. 69, no. 11, pp. 10969–10983, Nov. 2022.
[27] F. Gao, Z. Yin, C. Bai, D. Yuan, and J. Liu, "Speed sensorless control method of synchronous reluctance motor based on resonant Kalman filter," *IEEE Trans. Ind. Electron.*, vol. 70, no. 8, pp. 7627–7641, Aug. 2023.
[28] X. Yang, H. Hu, H. Hu, Y. Liu, and Z. He, "A quasi-resonant extended state observer-based predictive current control strategy for three-phase PWM rectifier," *IEEE Trans. Ind. Electron.*, vol. 69, no. 12, pp. 13910–13917, Dec. 2022.
[29] M. Tian, B. Wang, Y. Yu, Q. Dong, and D. Xu, "Adaptive active disturbance rejection control for uncertain current ripples suppression of PMSM drives," *IEEE Trans. Ind. Electron.*, vol. 71, no. 3, pp. 2320–2331, Mar. 2024.
[30] Z. Wang, K. Yu, Y. Li, and M. Gu, "Position sensorless control of dual three-phase IPMSM drives with high-frequency square-wave voltage injection," *IEEE Trans. Ind. Electron.*, vol. 70, no. 10, pp. 9925–9934, Oct. 2023.
[31] X. Zhang, Q. Xu, Y. Wang, and L. Luo, "A new adaptive dead time compensation method for dual three-phase permanent magnet synchronous motor," *Energy Rep.*, vol. 9, pp. 267–277, Nov. 2023.
[32] M. Hu, W. Hua, C. Cheng, Y. Wang, and C. Lu, "Discrete-time frequency-domain disturbance observer to mitigate harmonic current in PMSM drives and the implementation with reduced delay," *IEEE Trans. Power Electron.*, vol. 38, no. 8, pp. 9482–9493, Aug. 2023.
[33] Y. Zhang, J. Jin, and L. Huang, "Model-free predictive current control of PMSM drives based on extended state observer using ultralocal model," *IEEE Trans. Ind. Electron.*, vol. 68, no. 2, pp. 993–1003, Feb. 2021.
[34] A. G. Yepes, F. D. Freijedo, Ó. Lopez, and J. Doval-Gandoy, "High-performance digital resonant controllers implemented with two integrators," *IEEE Trans. Power Electron.*, vol. 26, no. 2, pp. 563–576, Feb. 2011.

Xuefeng Zhang (Student Member, IEEE) was born in Anhui, China, in 1995. He received the B.S. degree in automotive engineering from Chang'an Universuty, Xi'an, China, in 2018, and the M.S. degree in automotive engineering from Chongqing University, Chongqing, China, in 2021. He is currently working toward the Ph.D. degree in electrical engineering with the Chongqing University.

His current research interests include power electronic and advanced control of PMSM drives.

Qiwei Xu was born in Heilongjiang, China, in 1983. He received the B.S., M.S., and Ph.D. degrees from the Harbin Institute of Technology, Harbin, China, in 2006, 2008, and 2013, respectively, all in electrical engineering.

He is currently an Associate Professor with Chongqing University, Chongqing, China. His current research interests include design and control of special electric machines, electric drive systems of electric vehicles, and control and simulation of hybrid electric vehicles.

Yiru Miao was born in Inner Mongolia, China, in 1988. He received the B.S. degree in electrical engineering and automation from Xihua University, Chengdu, China, in 2009, the M.S. degree in electrification and automation of rail transit electrical from Southwest Jiaotong University, Chengdu, China in 2012, and the Ph.D. degree in electrical engineering from Chongqing University, Chongqing, China in 2019.

He is currently an Associate Researcher with Chongqing University, Chongqing, China. His research interests include power electronics and motor control technology.

Xuan Wu was born in Hunan, China, in 1983. He received the M.S. and Ph.D. degrees in automation from the College of Electrical and Information Engineering, Hunan University, Changsha, China, in 2011 and 2016, respectively.

He is currently an Associate Professor with the College of Electrical and Information Engineering, Hunan University. His research interests include permanent magnet synchronous motor drives, position sensorless control of AC motors.

Yiming Wang (Student Member, IEEE) was born in Chongqing, China, in 1985. He received the B.S. degree in exploration guidance and control from Beijing Institute of Technology, Beijing, China, in 2006, and the M.S. degree in electrical engineering from Chongqing University, Chongqing, China, in 2018. He is currently working toward the Ph.D. degree in electrical engineering with the Chongqing University.

His research interests include modern predictive control and sensorless control for electrical machine drive system.

Liangwu Yi was born in Chongqing, China, in 1999. He received the B.S. degree in electrical engineering from the School of Electrical Engineering, Chongqing University, Chongqing, China, in 2022. He is currently working toward the M.S. degree in electrical engineering with Chongqing University, Chongqing, China.

His research interests include the control of multiphase permanent magnet synchronous motors.